

**Title:** Nanodisc, amphipol or detergent belts in cryoEM reconstructions of membrane proteins are similar and correspond to a common ordered solvent layer

Veronica Zampieri<sup>1</sup>, Alexia Gobet<sup>1</sup>, Xavier Robert<sup>1</sup>, Pierre Falson<sup>1</sup>, Vincent Chaptal<sup>1\*</sup>

<sup>1</sup> Molecular Microbiology and Structural Biochemistry Laboratory (CNRS UMR 5086), University of Lyon, IBCP, 7, passage du Vercors, 69367 Lyon, France.

\* To whom correspondence should be addressed. [vincent.chaptal@ibcp.fr](mailto:vincent.chaptal@ibcp.fr)

## Summary

To maintain membrane proteins soluble in aqueous solution, amphipathic compounds are used to shield the hydrophobic patch of their membrane insertion, which forms a belt around the protein. This hydrophobic belt is seldom looked at due to the difficulty to visualize it. Cryo-EM is now offering this possibility, where belts are visible in 3D reconstructions. We investigated membrane proteins solved in nanodiscs, amphipols or detergents to analyze whether the nature of the amphipathic compound influences the belt size in 3D reconstructions. We identified belt boundaries in map-density distributions and measured distances for every reconstruction. We showed that all the belts create on average similar reconstructions, whether they originate from the same protein, or from protein from different shapes and structures. There is no difference among detergents or types of nanodisc used. These observations illustrate that the belt observed in 3D reconstructions corresponds to the minimum ordered layer around membrane proteins.

## 1. Introduction

Membrane protein structure determination has become almost a routine job with the recent development of single particle electron microscopy in cryogenic conditions (Cryo-EM). A skyrocketing amount of membrane protein structures becomes available improving our knowledge of many biological processes. In order to achieve this grail of a nice quality structure, it is necessary to extract the protein from the native membrane, and purify it to homogeneity so it can be applied on a grid and imaged on a microscope. And there lies the specificity of membrane proteins: they display a part of their structure that spans the membrane, abundant in hydrophobic residues, rendering them insoluble in water. There is thus a need for some amphipathic compound to shield this trans-membrane region from water and from other hydrophobic molecule or even other proteins around, else the result will be aggregation and loss of the precious gem.

Many recipes are available today to maintain membrane proteins in solution. The historical way, still very much used today, is to use detergents to extract membrane proteins from the membrane and then purify them in detergent solutions. Detergents are small molecules that display a hydrophilic head and a hydrophobic tail. Both moieties vary in nature, length and size allowing a large panel of possible screening for good conditions, and they are also sometimes used in mixtures[1]. By nature, detergents are very mobile and form a dynamic belt wrapping around the trans-membrane part of the protein[2]. Due to this dynamic property, detergents can have sometimes negative impacts on membrane proteins structure and function. Therefore, detergents with increased stabilizing properties have been more recently conceived for limiting such mobility either by having a design close to lipids (LMNG)[3] or by generating specific interactions[4]. Also, their amphipathic nature is unique to stabilize given conformations. Other tools have been developed to forgo the need for detergents. Among them the derivation of the lipid A apolipoprotein engineered as a series of Membrane Scaffold Proteins (MSP), that together with lipids and the membrane protein will form a lipidic nanodisc is a real success, allowing to reconstitute a more native environment and/or to vary the type of lipids around the membrane protein[5]. In the same vein, amphipols are polymers that wrap around purified membrane proteins and stabilize them without the need for detergents and lipids[6]. All these tools have been used for membrane protein structure determination by Cryo-EM. More recently, new polymers have been designed to directly extract membrane proteins from native membranes, allowing their purification without detergents[7, 8].

All these compounds generate a local amphipathic environment around the membrane region of membrane proteins that maintains them in aqueous solutions. This layer is a belt from which membrane proteins are indissociable. This solvent is however seldom looked at despite its huge influence on the protein function, due to the difficulty to visualize it. Cryo-EM now allows for the visualization of a layer wrapping around the transmembrane region of membrane proteins. We have taken this opportunity to investigate if there is an influence of these different amphipathic belts on their visualization after 3D reconstructions. We identified the position of the hydrophobic solvent belt in map-density distributions and measured the belts for many different proteins solved in nanodiscs, amphipols and detergents. We showed that all the belts create on average similar reconstructions, whether they originate from the same protein, or from protein from different shapes and structures. There is no difference amongst detergents or type of nanodisc used. These observations illustrate that the averaging procedure of CryoEM reconstructions returns a belt corresponding to a common minimum ordered solvent layer amongst all the membrane proteins particles

selected for this reconstruction. This solvation layer is however much smaller than the total amount of amphipathic compound embarked around membrane proteins.

## 2. Results

### 2.1. 3D reconstructions of membrane proteins structures solved by cryo-EM in several amphipathic belts

In order to discriminate whether there is an influence of the type of amphipathic belt on the 3D reconstructions used to image membrane proteins by cryo-EM, we have screened the whole Protein Data Bank to select for comparison the membrane proteins that have been solved only in multiple hydrophobic environments: nanodiscs, amphipols or detergents (Fig. 1A. and STable 1.). The idea behind this selection is to keep the protein fold constant in order to normalize its influence on the reconstruction, and to be able to focus on the solvent belts alone. The identification of the belt is obvious to a trained eye, capable of detecting the trans-membrane parts of a protein in a structure. The hydrophobic belt is characterized by an expansion of lower-level density in the vicinity of the membrane region as a decrease in the map density. After the observation of map-density distributions of each structure of this dataset, an apparent feature was observable to identify the belt and is exemplified in Figure 1B. At high density levels, the very ordered parts of the structure are visible, on which reconstruction was anchored. Typically, trans-membrane helices are key features used in 3D reconstructions of membrane proteins and are visible at this level. With decreasing density levels, the number of voxels increases in a concave shape (level 0). The higher ordered layers of the belt start to appear when the curve becomes convex (level 1, dotted arrow). The belt becomes more and more apparent over the course of about one log when the curve inflexes concavely (level 2) before a sharp increase in number of voxels leading to appearance of low-level noise throughout the box (level 3). Across all reconstructions, it is apparent that the more visible the hydrophobic belt, the clearer and sharper the transition is between levels 1 and 2.

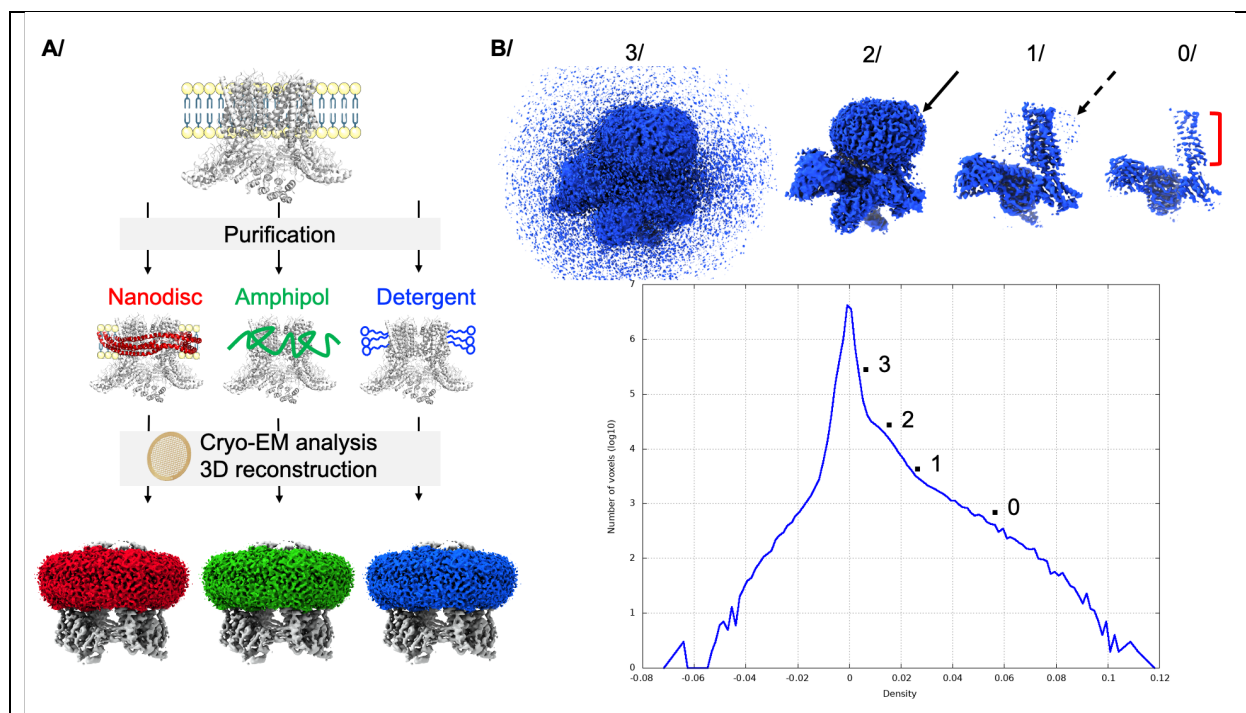
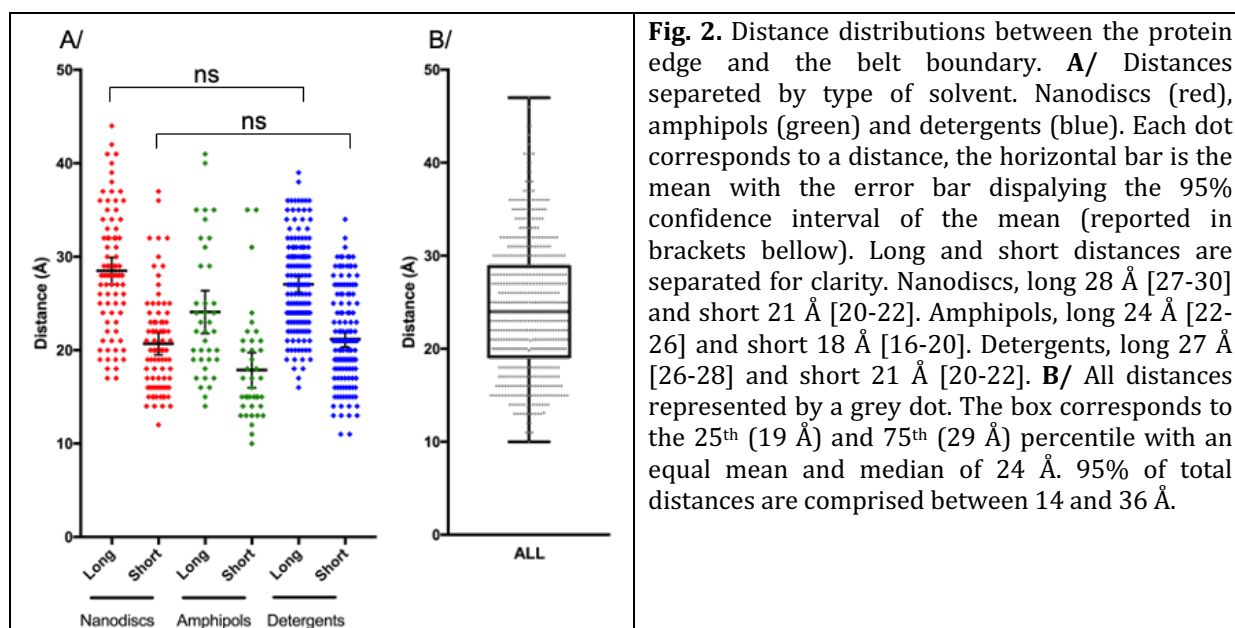


**Fig. 1.** Visualization of the different types of hydrophobic belts surrounding membrane proteins. **A/** General scheme of membrane protein purification from the membrane, kept in detergent (blue) or reconstituted in nanodisc (red) or amphipol (green), and imaged by cryo-EM to obtain a 3D reconstruction. The channel TRPV1 is used as an example of reconstruction (EMD-8117), with belts colored accordingly. **B/** Typical map-density distribution and representative density levels of reconstructions (EMD-20079). Level 0 corresponds to parts of the structure with strong density; the red bar shows the trans-membrane domain. Level 1 corresponds to the appearance of high density for the belt, depicted by the dotted arrow. Level 2 represents the maximum density observed at low-level density, depicted by the solid arrow. Level 3 corresponds to low density noise.

## 2.2. 3D reconstructions of membrane proteins in nanodiscs or detergents yield similar average belt sizes

Using the map-density histogram, we measured for each entry the belt size by determining the distance between the protein edge and the solvent boundaries at level 2 (SFig. 2 to 16., STable 2.). Belt reconstructions are not spherical but rather follow the protein shape. We could thus identify large and small distances of the hydrophobic solvent belt, which we separated in two categories for further processing. Figure 2 displays the distance distribution plot of all proteins separated by hydrophobic environments: nanodiscs, amphipols and detergents. For each type of belt, there is an apparent spread of distances, with 95% of total distances comprised between 14 and 36 Å, and no distances below 10 Å around the protein. Statistical analysis of long distances observed in detergents and nanodiscs show that they follow the same distribution, as well as small distances for these two categories. On average, the solvent belt is visible around the protein for 21 to 27 Å. The smaller amount of structures solved using amphipols precludes the statistical analysis on means using parametric statistics. Non-parametric statistics on ranks reveals first an ambiguity about long amphipol distances where the current data set cannot distinguish whether the distances are different or similar (more measurements on more structures are needed to solve the debate), and second unambiguously state that short distances measured in amphipols follow the same distribution as the nanodiscs or detergents ones. Put together, these results point to a common average distance distribution of solvent belts surrounding membrane protein observed after 3D reconstruction of cryo-EM data.

In order to distinguish if there is some inter-family of inter-solvent specificities hidden within the global distribution, we further separated proteins for individual analysis.



### 2.3. The TRPV family

The Transient Receptor Potential Vanilloid (TRPV) family consists of six ion channels, varying in ion-selectivity according to the sub-family. Despite being functionally distinct, they share a highly conserved fold, being active as a tetramer formed around 6 trans-membrane helices per monomer[9]. In the present dataset, we identified structures of TRPV1 in nanodiscs and amphipols, TRPV2 in nanodiscs, amphipols and detergents (LMNG and DMNG), and TRPV5 in nanodiscs and DMNG (STable 1.). The fact that TRPV proteins share a conserved fold gives a unique opportunity to compare varying hydrophobic solvent belts. To these proteins, we also included structures of TRPV3 and 6 that were solved in only one type of amphipathic solvent, benefiting from the fact that they share the same fold.

The signal of the hydrophobic belt varies in intensity among the different 3D reconstructions, for unclear reasons (Fig. 3A., SFig. 2-5.). For example, the nanodisc belt of TRPV1 and 2 appears with a strong signal in these five reconstructions, while its intensity is much milder in the two reconstructions of TRPV5. Similar trends can be seen in amphipols or detergents across the various reconstructions. Nevertheless, belt boundaries are clearly visible and were measured for all thirty proteins (Fig. 3C.) Distance distributions follow a similar trend as the global one (Fig. 2A.), where differences amongst belts are undistinguishable. The same ambiguity remains between long distances of nanodiscs and amphipols, but it is challenged by the lack of difference this time between amphipols and detergents. More measures on more reconstructions would help to differentiate the trend. Nevertheless, the fact that short distances show the same distributions across the three types of solvent and the undistinguishable long distances for nanodiscs and detergents suggest a similar average size for solvent belts around TRPV proteins.



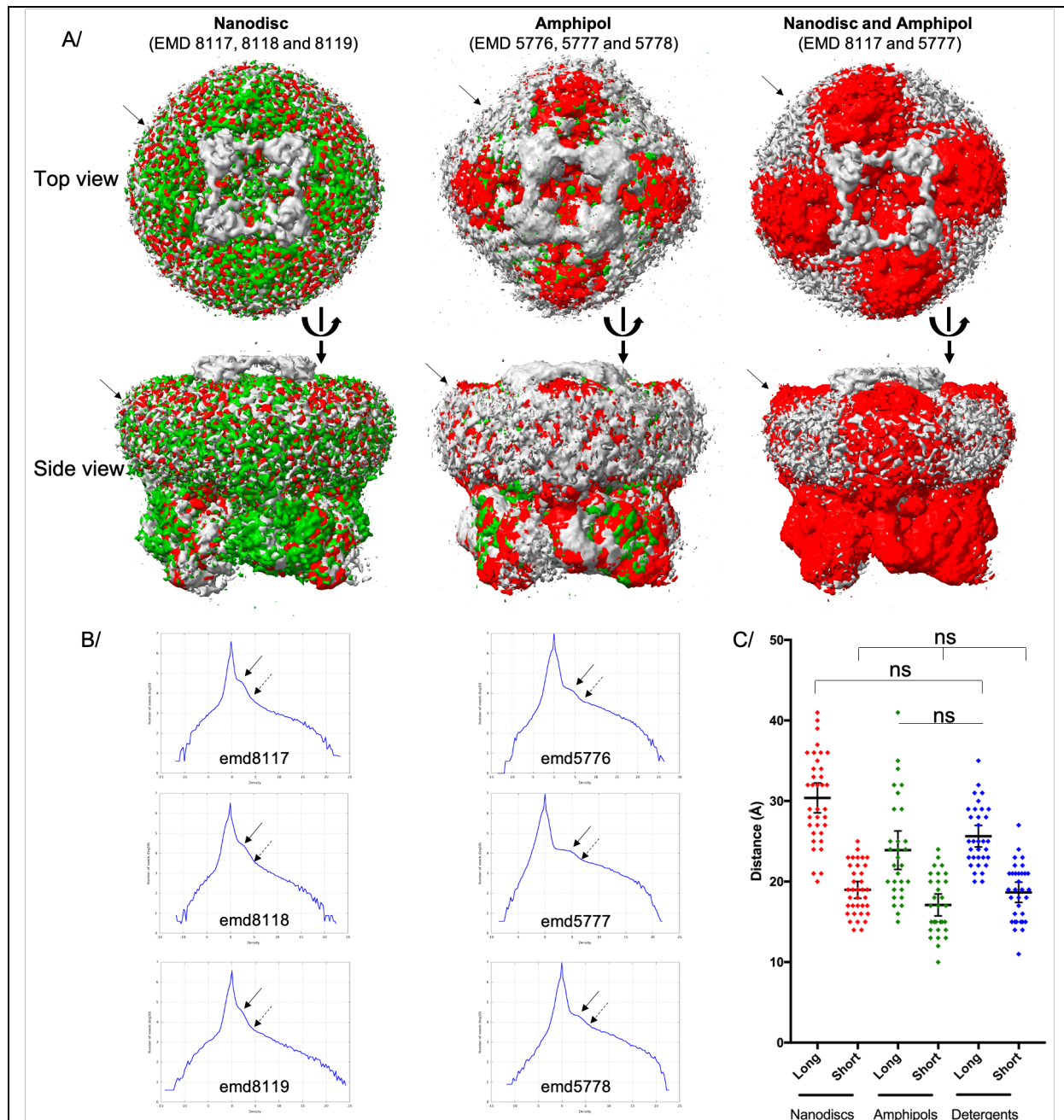
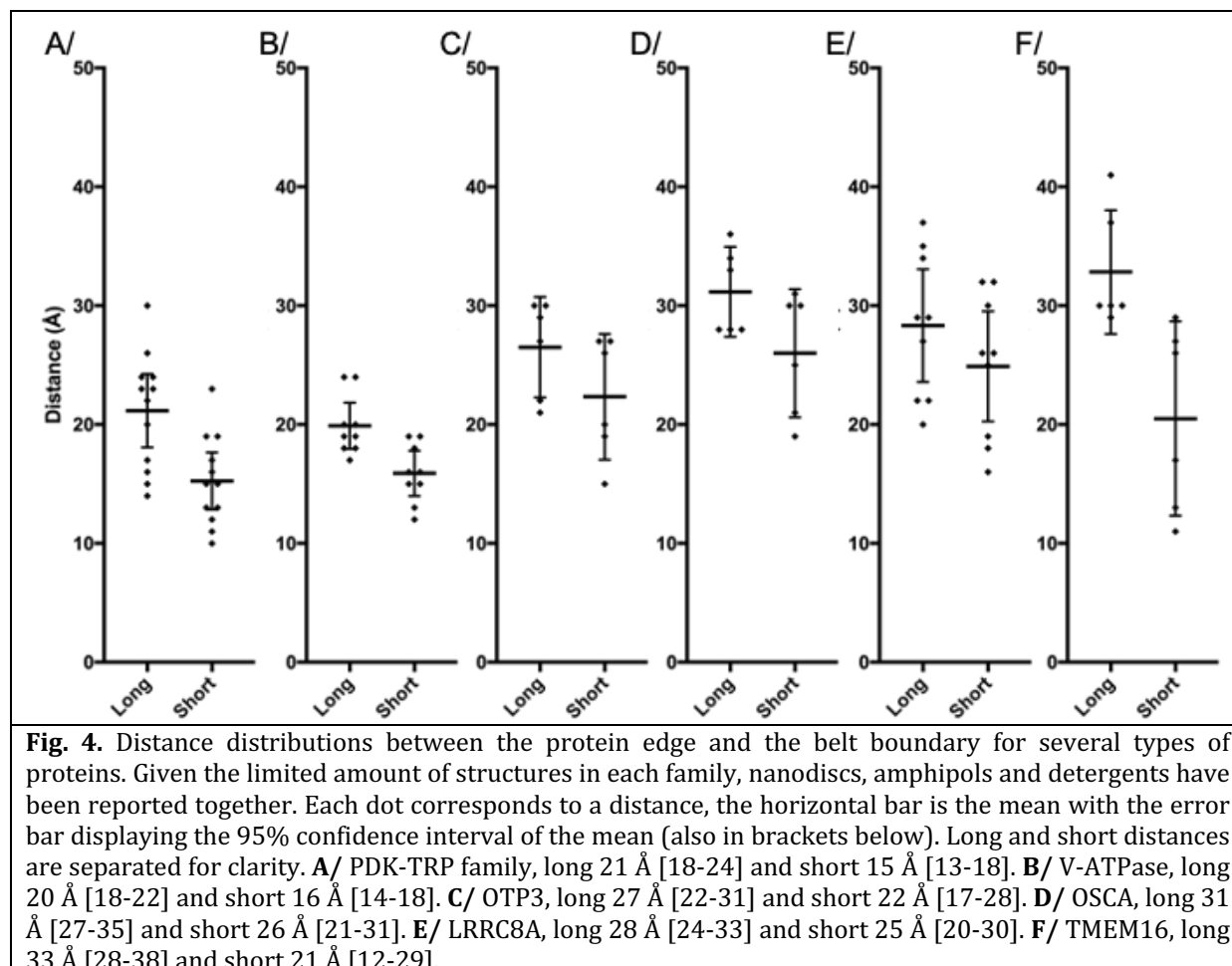


**Fig. 3.** Belts surrounding TRPV proteins. **A/** Example of the TRPV1 proteins solved in nanodisc or amphipols. The EMD accession codes are listed and each structure are colored in grey, red or green, and overlaid. Top and side views are depicted, the solid arrow points to the position of the solvent belt. **B/** Map-density distribution for each entry. On each distribution, the dotted arrow shows the belt appearance at level 1, and the solid arrow at level 2. **C/** Distance distributions for all TRPV proteins, with the same color-coding as Fig.2. Statistical analysis was carried out using ANOVA and Kruskal-Wallis.

#### 2.4. Similar average belts length across multiple protein types solved using different amphipathic solvents

We have identified in the dataset multiple protein structures that have been solved only a few times in different hydrophobic belts. The limited amount of structures prevents a statistical analysis on each protein. Instead, these proteins were evaluated in a group, thereby offering the opportunity to compare proteins with completely distinct folds, and originating from various sources and amphipathic environments (Fig. 4.,

STable 1., SFig. 6-11.). Within each protein, the hydrophobic belt distances cluster rather well, showing a narrow distribution of distances, sampling apparently randomly across the distribution of all proteins shown in Fig. 2. Comparison of all these proteins reveals that their means group in similar ranges, with overlapping confidence interval of the mean, invoking a comparable hydrophobic belt around all these proteins.

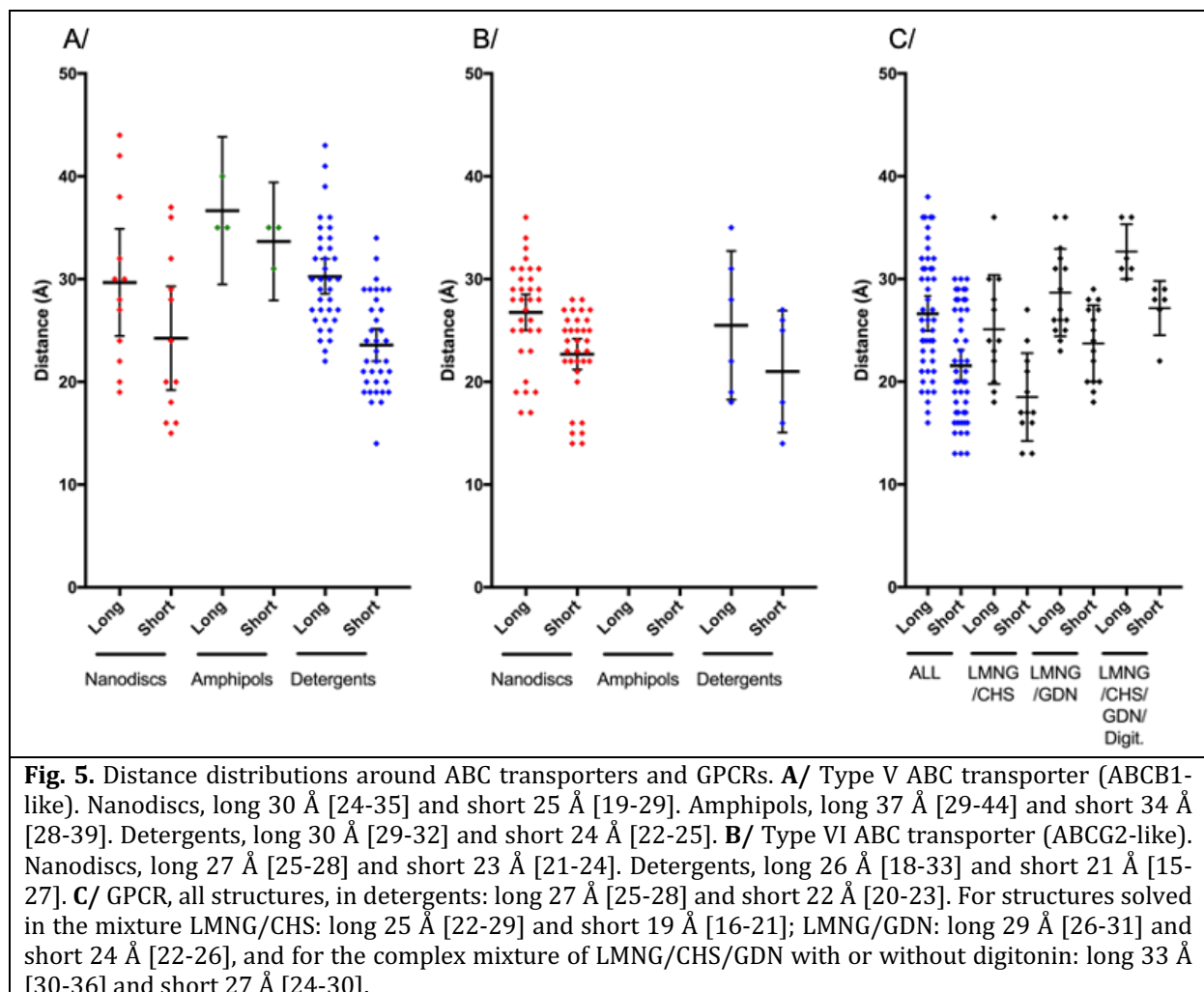


## 2.5. The superfamily of ABC transporters

ATP-binding Cassette (ABC) transporters are a large superfamily of transporters, harnessing the energy of ATP-binding and hydrolysis to translocate a wide range of substrate across many biological membranes. They are ubiquitous, and involved in many important cell-homeostasis functions[10]. While no single ABC transporter has been solved by cryo-EM in different hydrophobic environment, these proteins display a common fold and all together have been solved in nanodiscs, amphipols and detergents. They also offer the advantage that there is a large amount of structures, solved by several groups around the world using their own methodologies, and that their structures have been solved in multiple conformations offering a unique view of the solvent distribution around proteins in motion. Type I (or Type-V exporter, ABCB1-like) and type II (or Type-VI exporter, ABCG2-like) have been separated for clearer analysis (Fig. 5AB., SFig. 12-14.). Within the type I, no difference is detected between the distance distributions. Between type I and II, the distances are also inseparable, claiming that the



hydrophobic belt around ABC transporters is always of similar size, regardless of the conformation or the arrangement of trans-membrane helices.



## 2.6. Similar detergent belt reconstructions around GPCRs

Twenty one unique structures of GPCR were found in the present database, belonging to the A, B, C or F classes (or G, R, F or S, respectively, according to the GRAFS nomenclature[11]), all solved in detergents. The vast majority used LMNG as a base, alone or in combination with other cholesterol-like detergents such as CHS, GDN or digitonin. All structures have been solved in complex with their cognate G proteins, and/or  $\beta$ -arrestin, in various flavors. Like for ABC transporters, all these GPCR structures share an overall fold that grants the direct comparison of their associated belts, with local differences between structures making it more worthwhile to analyze differences in the detergent belt measurements. The detergent belt distance distribution (Fig. 5., SFig. 15-16.) is inseparable from the ABC transporter ones, or from the global distance distribution of all membrane proteins solved by cryo-EM (Fig. 2.). Following this trend, the popular detergent mixes, for these GPCR structures, between LMNG and CHS, GDN or digitonin yield similar detergent belt reconstructions, on average.

## 2.7. Different types of nanodiscs yield similar reconstructions; detergent belts are all of equivalent sizes.

We checked whether a difference in distance distribution can be observed among the type of hydrophobic solvent. For instance, different flavors of Membrane Scaffold Proteins (MSP) are available to form nanodiscs, varying the length of a helical fragment within the MSP to make it longer or shorter[5]. In the current dataset, proteins have been solved with 3 types of MSP, the short MSP1D1 and its longest version MSP1E3D1 comprising 3 helical insertion. MSP2N2 is formed by the fusion of two MSP1D1. Figure 6A shows the distance distribution of the nanodisc belts sorted by nanodisc type, revealing that they are undistinguishable after reconstruction. Long and short distances of two types of nanodiscs formed by MSP1D1 and MSP2N2 follow the same distribution, with means equivalent to the mean obtained for all measurements in Fig. 2. Following this observation, distances were also separated by type of detergent to distinguish if a detergent or a detergent mixture can give rise to distinct size of belts. Distances measured from different types of detergents are all virtually indistinguishable, and distribute in the same range as distances observed for nanodiscs and all other measurements together (Fig. 2.).

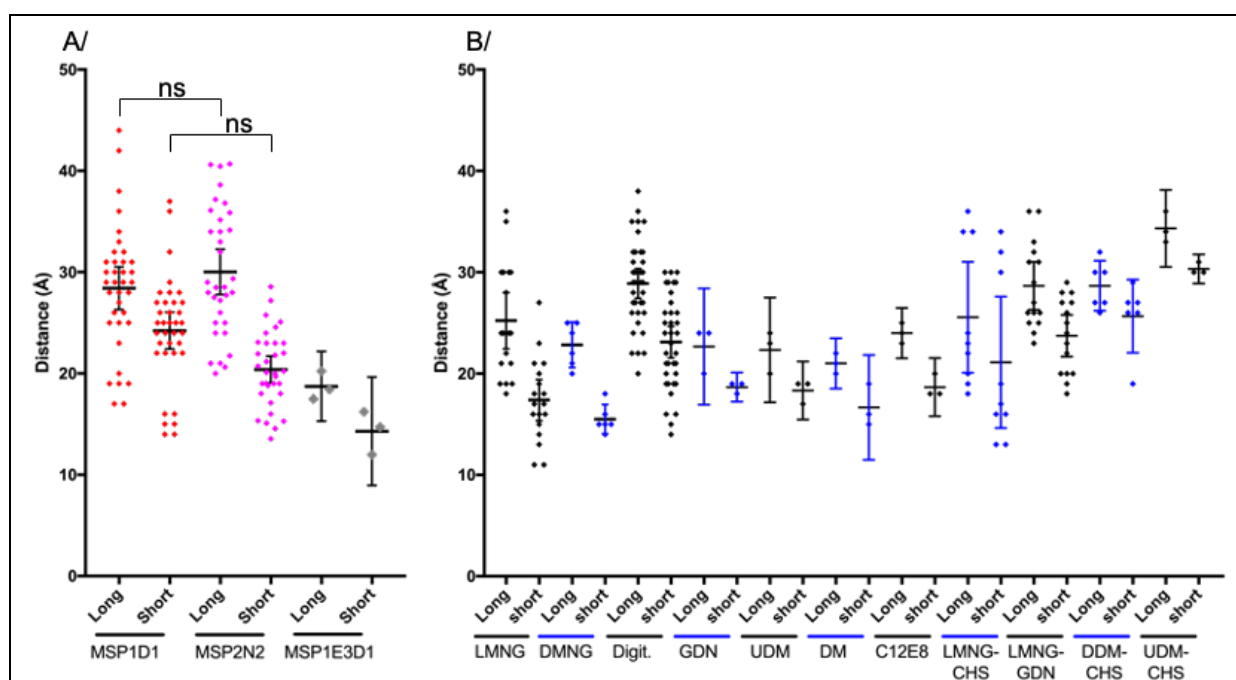


**Fig. 6.** Distance distributions of the different nanodiscs or detergents belts. **A/** Distances measured for nanodiscs belts. MSP1D1, long 28 Å [26-31] and short 24 Å [22-26]. MSP2N2, long 32 Å [30-35] and short 20 Å [18-22]. MSP1E3D1, long 19 Å [15-22] and short 14 Å [9-20]. **B/** Distances measured for the most represented detergents in this dataset. LMNG (Lauryl Maltose Neopentyl Glycol), long 25 Å [22-28] and short 17 Å [15-19]. DMNG (Decyl Maltose Neopentyl Glycol), long 23 Å [20-25] and short 16 Å [14-18]. Digit. (Digitonin), long 29 Å [27-30] and short 23 Å [22-25]. GDN (Glyco-diosgenin), long 23 Å [17-28] and short 19 Å [17-20]. UDM (Undecyl-β-D-galactopyranoside), long 22 Å [17-28] and short 18 Å [15-21]. DM (Decyl-β-D-galactopyranoside), long 21 Å [19-24] and short 17 Å [12-22]. C12E8 (Octaethylene Glycol Monododecyl Ether), long 24 Å [22-27] and short 19 Å [16-22]. LMNG-CHS (CHS: Cholesteryl-hemisuccinate), long 26 Å [20-31] and short 21 Å [15-28]. LMNG-GDN, long 29 Å [26-31] and short 24 Å [22-26]. DDM-CHS (DDM: Dodecyl-β-D-galactopyranoside), long 29 Å [26-31] and short 26 Å [22-29]. UDM-CHS, long 34 Å [31-38] and short 30 Å [29-32]. Numbers are the mean followed by the 95% confidence interval of the mean in brackets.

### 3. Discussion

In order to discriminate if the compounds used to shield the membrane region of a membrane proteins have an influence on the observation of the corresponding belt by cryo-EM, we performed a statistical analysis of a curated database of selected membrane proteins solved in several hydrophobic environments. By visualizing every structure, we were able to identify in map-density distributions a signature of hydrophobic belt appearance (levels 1 & 2 in Fig. 1B.). We further identified its boundaries for every protein and measured its size for statistical analysis. 95% of all measured lengths distribute between 14 and 36 Å around the surface of trans-membrane segments, and half of the belts are comprised between 19 and 29 Å. The hydrophobic belts were further separated by type of solvent to probe whether nanodiscs, amphipols or detergents can yield tighter or larger belts. The results presented in Figure 2 show that these three types of solvent were following the same distributions, and were therefore statistically indistinguishable on average.

This result correlates well with other types of measurements of the same solvents by other methods. Molecular dynamics simulations of membrane proteins embedded in amphipols or detergents show a belt around the transmembrane regions, with some degree of flexibility[2, 12-14]. Indeed, the belt formed by these amphipathic compounds is very fluid, revealing local clusters of individual molecules, forming and deforming with time. When measured using neutron diffraction of membrane protein crystals[15], an averaging technique like cryo-EM, the detergent belt appears as a homogeneous belt around the protein. The size of the belt observed was then highly dependent on the type of crystal as the detergent could merge between belts of symmetric molecules[16]. All these techniques have been limited to the size of the system for molecular dynamic simulations, or “neutron-diffraction quality” crystals combined with deuterated detergents; here, cryo-EM allows for the visualization of any amphipathic compound, with belt measurements matching other measuring methods.

Since the hydrophobic belt has intrinsic properties to diffract electrons, it has a strong influence on the reconstructions. For example, for a 130 kDa ABC transporter, the DDM belt (400 monomers) accounts for an additional 200 kDa[2]. It is thus understandable that even if this detergent belt is not ordered, it still influences electron diffraction around the membrane protein, nicely exemplified with 3D variability of the detergent belt has been visualized in cryo-EM[17].

Nanodiscs formation with a membrane protein embedded is in itself a stunning process, where the three ingredients (Membrane Scaffold Protein, lipids and membrane protein) are mixed together, and detergents removed using biobeads. The membrane protein embedded into nanodiscs are then separated from empty nanodiscs using affinity chromatography and/or size exclusion chromatography. The object comprising the membrane protein of interest is in reality quite heterogeneous, containing a mixture of large and small nanodiscs, with more or less lipids embarked. Also, within the nanodisc, the membrane protein can move from side to side and does not always stay in the middle. This explains why the membrane scaffold protein is hardly observed in 3D reconstructions of membrane proteins in nanodiscs.

Following this idea, we further explored if we could identify within a set of protein, or type of amphipathic compound, a combination that could influence the size of the solvent belt seen around membrane proteins. We could not establish any significant difference in the measurement distributions, all falling within the overall distribution described in Figure 2. Hereabouts, the incorporation of ABC transporters and GPCRs in

this dataset yields an important viewpoint. From detergent quantification we know that the amount of detergent present around membrane proteins is directly proportional to the accessible hydrophobic area[2]. The amount of detergent around ABC transporters (12 trans-membrane helices) is thus inherently larger than the one around GPCRs (7 trans-membrane helices). One would thus expect to visualize a larger belt around ABC transporters by cryo-EM, but the size of the belt is on the contrary following the same distribution (Fig. 5.).

Finally, there is the observation that the solvent belt observed around membrane proteins by cryo-EM is circular, somewhat reminiscent of the ones observed by neutron diffraction of crystals. This is partly due to symmetries enforced during reconstructions, but at the heart, mostly due to particle averaging. Particle alignments are anchored on secondary structures, among which trans-membrane helices are a lighthouse in a fog of amphipathic solvent. The solvent observed during reconstruction is thus made out of several layers distributing radially away from the protein boundary (Fig. 7.). Level 1 corresponds to the highest density, and represents the common minimum ordered layer, where the amphipathic compound is always present around the membrane protein. This layer concomitantly increases in size and decreases in density as it radiates away from the protein boundary, representing areas of space less and less populated by the solvent. This is influenced by the fluid properties of the solvent, as the sample is vitrified in liquid ethane. Each individual particle of a dataset represents a snapshot carrying its own belt-distribution. These observations reinforce the idea that the belt visualized by cryo-EM is a fraction of the volume occupied by the hydrophobic belt and represents the common minimum ordered solvent surrounding the protein.

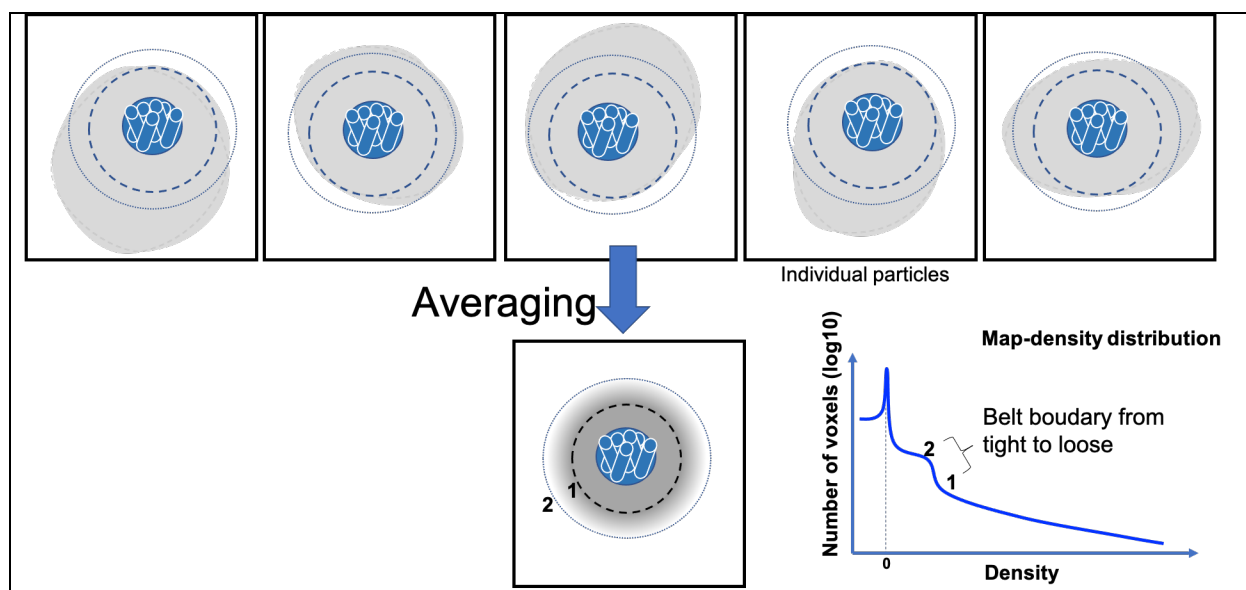


**Fig. 7.** Influence of the averaging on hydrophobic solvent visualization. Top: set of particles all centered on the trans-membrane helices, with the same orientation. The inner dash circle represents the volume around the membrane protein where the hydrophobic solvent is always present. The outer dotted circle represents the spread upto where the solvent belt can be visualized. The solvent is shown in gray, with various shapes to highlight its variability around the trans-membrane domain. Bottom: The result of the averaging is a clear definition of transmembrane helices, and a gradient of presence for the solvent radiating away from the protein boundary. The level 1 and 2 correspond to the levels presented on the map-density distribution.

## 4. Material and methods

### 4.1. Membrane proteins structure database extraction

Based on the mpstruc database (<https://blanco.biomol.uci.edu/mpstruc/>) that lists all the membrane proteins of known 3D structure, we created a dataset containing only entries solved by Cryo-EM, as of January 17<sup>th</sup>, 2020. We wrote a Bash shell script in order to automatically extract information from these entries. This allowed us to determine those which have been solved in multiple hydrophobic environments (nanodiscs, amphipols or detergents) and to sort them in distinct subsets. Then, for each entry, we extracted from the Electron Microscopy Data Bank (EMDB) the map-density distribution data in order to render graphs plotting the density distribution (*i.e.* the number of voxels as a function of the density).

### 4.2. Map comparison

Maps were retrieved from EMDB and opened in ChimeraX[18]. Maps were first manually aligned, then aligned using the volume tool within ChimeraX. Threshold levels to compare the maps were adjusted to include the highest level of low contour information (level 2 in Fig 1B), without including noise voxels appearing in the box.

### 4.3. Measures of the solvent belt around the protein

The measure of solvent belt thickness was performed in ChimeraX using the tool “tape” which is included in the software. The density map histogram was used to increase or decrease the contour information. At first, the density map showed the maximum of the solvent belt information (Level 2) and vertical lines were drawn to signal the limit the solvent belt. Then the density map contour was reduced in order to see clearly the protein density (Level 0). Horizontal lines were drawn to link the vertical lines and the protein density. The tape tool measured the distance. This experiment was performed six times and in distinct positions of the solvent belt.

### 4.4. Statistical analysis

Statistical analysis (Prism.v7.2) was performed only when the amount of measures was sufficient to perform meaningful statistics. For this reason, some measures in amphipols or on individual types of proteins or hydrophobic environments were excluded. ANOVA was used to distinguish differences between means, and Kruskal-Wallis was used to distinguish differences on ranks. For all figures, means were computed as well as the 95% confidence interval of the mean.

## Author contributions

XR extracted the database. VZ measured all distances. VZ, AG and VC created the figures and analysed the data. All authors wrote the manuscript.

## Acknowledgments

This work was supported by the CNRS, Lyon University and the French National Research Agency, ANR-CLAMP2- 18-CE11-0002-01 to PF and VC and ANR-19-CE11-0023-01 to VC and PF.

## References



1. Seddon, A.M., P. Curnow, and P.J. Booth, *Membrane proteins, lipids and detergents: not just a soap opera*. Biochim Biophys Acta, 2004. **1666**(1-2): p. 105-17.
2. Chaptal, V., et al., *Quantification of Detergents Complexed with Membrane Proteins*. Sci Rep, 2017. **7**: p. 41751.
3. Chae, P.S., et al., *Maltose-neopentyl glycol (MNG) amphiphiles for solubilization, stabilization and crystallization of membrane proteins*. Nat Methods, 2010. **7**(12): p. 1003-8.
4. Nguyen, K.A., et al., *Glycosyl-Substituted Dicarboxylates as Detergents for the Extraction, Overstabilization, and Crystallization of Membrane Proteins*. Angew Chem Int Ed Engl, 2018. **57**(11): p. 2948-2952.
5. Bayburt, T.H. and S.G. Sligar, *Membrane protein assembly into Nanodiscs*. FEBS Lett, 2010. **584**(9): p. 1721-7.
6. Marconnet, A., et al., *Solubilization and Stabilization of Membrane Proteins by Cycloalkane-Modified Amphiphilic Polymers*. Biomacromolecules, 2020.
7. Oluwole, A.O., et al., *Solubilization of Membrane Proteins into Functional Lipid-Bilayer Nanodiscs Using a Diisobutylene/Maleic Acid Copolymer*. Angew Chem Int Ed Engl, 2017. **56**(7): p. 1919-1924.
8. Dörr, J.M., et al., *The styrene-maleic acid copolymer: a versatile tool in membrane research*. Eur Biophys J, 2016. **45**(1): p. 3-21.
9. van Goor, M.K., et al., *High-resolution structures of transient receptor potential vanilloid channels: Unveiling a functionally diverse group of ion channels*. Protein Sci, 2020. **29**(7): p. 1569-1580.
10. Thomas, C. and R. Tampé, *Structural and Mechanistic Principles of ABC Transporters*. Annu Rev Biochem, 2020. **89**: p. 605-636.
11. Fredriksson, R., et al., *The G-Protein-Coupled Receptors in the Human Genome Form Five Main Families: Phylogenetic Analysis, Paralogon Groups, and Fingerprints*. Molecular Pharmacology, 2003. **63**(6): p. 1256-1256-1272.
12. Perlmutter, J.D., J.-L. Popot, and J.N. Sachs, *Molecular Dynamics Simulations of a Membrane Protein/Amphipol Complex*. The Journal of Membrane Biology, 2014. **247**(9): p. 883-895.
13. Etzkorn, M., et al., *How Amphipols Embed Membrane Proteins: Global Solvent Accessibility and Interaction with a Flexible Protein Terminus*. The Journal of Membrane Biology, 2014. **247**(9): p. 965-970.
14. Wolfe, A.J., et al., *Quantification of Membrane Protein-Detergent Complex Interactions*. The Journal of Physical Chemistry B, 2017. **121**(44): p. 10228-10241.
15. Pebay-Peyroula, E., et al., *Detergent structure in tetragonal crystals of OmpF porin*. Structure, 1995. **3**(10): p. 1051-9.
16. Penel, S., et al., *Detergent binding in trigonal crystals of OmpF porin from Escherichia coli*. Biochimie, 1998. **80**(5-6): p. 543-51.
17. Punjani, A. and D.J. Fleet, *3D Variability Analysis: Directly resolving continuous flexibility and discrete heterogeneity from single particle cryo-EM images*. bioRxiv, 2020: p. 2020.04.08.032466.
18. Goddard, T.D., et al., *UCSF ChimeraX: Meeting modern challenges in visualization and analysis*. Protein Sci, 2018. **27**(1): p. 14-25.
19. Liao, M., et al., *Structure of the TRPV1 ion channel determined by electron cryo-microscopy*. Nature, 2013. **504**(7478): p. 107-12.
20. Cao, E., et al., *TRPV1 structures in distinct conformations reveal activation mechanisms*. Nature, 2013. **504**(7478): p. 113-8.

21. Gao, Y., et al., *TRPV1 structures in nanodiscs reveal mechanisms of ligand and lipid action*. Nature, 2016. **534**(7607): p. 347-51.
22. Pumroy, R.A., et al., *Molecular mechanism of TRPV2 channel modulation by cannabidiol*. Elife, 2019. **8**.
23. Zubcevic, L., et al., *Cryo-electron microscopy structure of the TRPV2 ion channel*. Nat Struct Mol Biol, 2016. **23**(2): p. 180-186.
24. Zubcevic, L., et al., *Symmetry transitions during gating of the TRPV2 ion channel in lipid membranes*. Elife, 2019. **8**.
25. Dosey, T.L., et al., *Structures of TRPV2 in distinct conformations provide insight into role of the pore turret*. Nat Struct Mol Biol, 2019. **26**(1): p. 40-49.
26. Huynh, K.W., et al., *Structure of the full-length TRPV2 channel by cryo-EM*. Nat Commun, 2016. **7**: p. 11130.
27. Singh, A.K., L.L. McGoldrick, and A.I. Sobolevsky, *Structure and gating mechanism of the transient receptor potential channel TRPV3*. Nat Struct Mol Biol, 2018. **25**(9): p. 805-813.
28. Shimada, H., et al., *The structure of lipid nanodisc-reconstituted TRPV3 reveals the gating mechanism*. Nat Struct Mol Biol, 2020. **27**(7): p. 645-652.
29. Zubcevic, L., et al., *Conformational ensemble of the human TRPV3 ion channel*. Nat Commun, 2018. **9**(1): p. 4773.
30. Deng, Z., et al., *Gating of human TRPV3 in a lipid bilayer*. Nat Struct Mol Biol, 2020. **27**(7): p. 635-644.
31. Singh, A.K., et al., *Structural basis of temperature sensation by the TRP channel TRPV3*. Nat Struct Mol Biol, 2019. **26**(11): p. 994-998.
32. Hughes, T.E., et al., *Structure-based characterization of novel TRPV5 inhibitors*. Elife, 2019. **8**.
33. Dang, S., et al., *Structural insight into TRPV5 channel function and modulation*. Proc Natl Acad Sci U S A, 2019. **116**(18): p. 8869-8878.
34. Singh, A.K., et al., *Structural bases of TRP channel TRPV6 allosteric modulation by 2-APB*. Nat Commun, 2018. **9**(1): p. 2465.
35. Kasuya, G., et al., *Cryo-EM structures of the human volume-regulated anion channel LRRC8*. Nat Struct Mol Biol, 2018. **25**(9): p. 797-804.
36. Kern, D.M., et al., *Cryo-EM structures of the DCPIB-inhibited volume-regulated anion channel LRRC8A in lipid nanodiscs*. Elife, 2019. **8**.
37. Kefauver, J.M., et al., *Structure of the human volume regulated anion channel*. Elife, 2018. **7**.
38. Dang, S., et al., *Cryo-EM structures of the TMEM16A calcium-activated chloride channel*. Nature, 2017. **552**(7685): p. 426-429.
39. Mazhab-Jafari, M.T., et al., *Atomic model for the membrane-embedded V(O) motor of a eukaryotic V-ATPase*. Nature, 2016. **539**(7627): p. 118-122.
40. Roh, S.H., et al., *The 3.5-Å CryoEM Structure of Nanodisc-Reconstituted Yeast Vacuolar ATPase V(o) Proton Channel*. Mol Cell, 2018. **69**(6): p. 993-1004.e3.
41. Vasanthakumar, T., et al., *Structural comparison of the vacuolar and Golgi V-ATPases from Saccharomyces cerevisiae*. Proc Natl Acad Sci U S A, 2019. **116**(15): p. 7272-7277.
42. Saotome, K., et al., *Structures of the otopetrin proton channels Otop1 and Otop3*. Nat Struct Mol Biol, 2019. **26**(6): p. 518-525.
43. Chen, Q., et al., *Structural and functional characterization of an otopetrin family proton channel*. Elife, 2019. **8**.

44. Jojoa-Cruz, S., et al., *Cryo-EM structure of the mechanically activated ion channel OSCA1.2*. Elife, 2018. **7**.
45. Maity, K., et al., *Cryo-EM structure of OSCA1.2 from Oryza sativa elucidates the mechanical basis of potential membrane hyperosmolality gating*. Proc Natl Acad Sci U S A, 2019. **116**(28): p. 14309-14318.
46. Shen, P.S., et al., *The Structure of the Polycystic Kidney Disease Channel PKD2 in Lipid Nanodiscs*. Cell, 2016. **167**(3): p. 763-773.e11.
47. Su, Q., et al., *Structure of the human PKD1-PKD2 complex*. Science, 2018. **361**(6406).
48. Grieben, M., et al., *Structure of the polycystic kidney disease TRP channel Polycystin-2 (PC2)*. Nat Struct Mol Biol, 2017. **24**(2): p. 114-122.
49. Wilkes, M., et al., *Molecular insights into lipid-assisted Ca(2+) regulation of the TRP channel Polycystin-2*. Nat Struct Mol Biol, 2017. **24**(2): p. 123-130.
50. Mi, W., et al., *Structural basis of MsbA-mediated lipopolysaccharide transport*. Nature, 2017. **549**(7671): p. 233-237.
51. Alam, A., et al., *Structural insight into substrate and inhibitor discrimination by human P-glycoprotein*. Science, 2019. **363**(6428): p. 753-756.
52. Kim, Y. and J. Chen, *Molecular structure of human P-glycoprotein in the ATP-bound, outward-facing conformation*. Science, 2018. **359**(6378): p. 915-919.
53. Alam, A., et al., *Structure of a zosuquidar and UIC2-bound human-mouse chimeric ABCB1*. Proc Natl Acad Sci U S A, 2018. **115**(9): p. E1973-e1982.
54. Fay, J.F., et al., *Cryo-EM Visualization of an Active High Open Probability CFTR Anion Channel*. Biochemistry, 2018. **57**(43): p. 6234-6246.
55. Zhang, Z., F. Liu, and J. Chen, *Molecular structure of the ATP-bound, phosphorylated human CFTR*. Proc Natl Acad Sci U S A, 2018. **115**(50): p. 12757-12762.
56. Liu, F., et al., *Molecular Structure of the Human CFTR Ion Channel*. Cell, 2017. **169**(1): p. 85-95.e8.
57. Zhang, Z. and J. Chen, *Atomic Structure of the Cystic Fibrosis Transmembrane Conductance Regulator*. Cell, 2016. **167**(6): p. 1586-1597.e9.
58. Liu, F., et al., *Structural identification of a hotspot on CFTR for potentiation*. Science, 2019. **364**(6446): p. 1184-1188.
59. Zhang, Z., F. Liu, and J. Chen, *Conformational Changes of CFTR upon Phosphorylation and ATP Binding*. Cell, 2017. **170**(3): p. 483-491.e8.
60. Johnson, Z.L. and J. Chen, *Structural Basis of Substrate Recognition by the Multidrug Resistance Protein MRP1*. Cell, 2017. **168**(6): p. 1075-1085.e9.
61. Johnson, Z.L. and J. Chen, *ATP Binding Enables Substrate Release from Multidrug Resistance Protein 1*. Cell, 2018. **172**(1-2): p. 81-89.e10.
62. Oldham, M.L., N. Grigorieff, and J. Chen, *Structure of the transporter associated with antigen processing trapped by herpes simplex virus*. Elife, 2016. **5**.
63. Taylor, N.M.I., et al., *Structure of the human multidrug transporter ABCG2*. Nature, 2017. **546**(7659): p. 504-509.
64. Jackson, S.M., et al., *Structural basis of small-molecule inhibition of human multidrug transporter ABCG2*. Nat Struct Mol Biol, 2018. **25**(4): p. 333-340.
65. Manolaridis, I., et al., *Cryo-EM structures of a human ABCG2 mutant trapped in ATP-bound and substrate-bound states*. Nature, 2018. **563**(7731): p. 426-430.
66. Qian, H., et al., *Structure of the Human Lipid Exporter ABCA1*. Cell, 2017. **169**(7): p. 1228-1239.e10.
67. Li, Y., B.J. Orlando, and M. Liao, *Structural basis of lipopolysaccharide extraction by the LptB(2)FGC complex*. Nature, 2019. **567**(7749): p. 486-490.

68. Tang, X., et al., *Cryo-EM structures of lipopolysaccharide transporter LptB(2)FGC in lipopolysaccharide or AMP-PNP-bound states reveal its transport mechanism*. Nat Commun, 2019. **10**(1): p. 4175.
69. Liang, Y.L., et al., *Phase-plate cryo-EM structure of a class B GPCR-G-protein complex*. Nature, 2017. **546**(7656): p. 118-123.
70. Liang, Y.-L., et al., *Cryo-EM structure of the active, Gs-protein complexed, human CGRP receptor*. Nature, 2018. **561**(7724): p. 492-497.
71. Kang, Y., et al., *Cryo-EM structure of human rhodopsin bound to an inhibitory G protein*. Nature, 2018. **558**(7711): p. 553-558.
72. Draper-Joyce, C.J., et al., *Structure of the adenosine-bound human adenosine A(1) receptor-G(i) complex*. Nature, 2018. **558**(7711): p. 559-563.
73. Liang, Y.L., et al., *Phase-plate cryo-EM structure of a biased agonist-bound human GLP-1 receptor-Gs complex*. Nature, 2018. **555**(7694): p. 121-125.
74. García-Nafria, J., et al., *Cryo-EM structure of the serotonin 5-HT(1B) receptor coupled to heterotrimeric G(o)*. Nature, 2018. **558**(7711): p. 620-623.
75. García-Nafria, J., et al., *Cryo-EM structure of the adenosine A(2A) receptor coupled to an engineered heterotrimeric G protein*. Elife, 2018. **7**.
76. Krishna Kumar, K., et al., *Structure of a Signaling Cannabinoid Receptor 1-G Protein Complex*. Cell, 2019. **176**(3): p. 448-458.e12.
77. Zhao, L.H., et al., *Structure and dynamics of the active human parathyroid hormone receptor-1*. Science, 2019. **364**(6436): p. 148-153.
78. Nguyen, A.H., et al., *Structure of an endosomal signaling GPCR-G protein- $\beta$ -arrestin megacomplex*. Nat Struct Mol Biol, 2019. **26**(12): p. 1123-1131.
79. Maeda, S., et al., *Structures of the M1 and M2 muscarinic acetylcholine receptor/G-protein complexes*. Science, 2019. **364**(6440): p. 552-557.
80. Kato, H.E., et al., *Conformational transitions of a neurotensin receptor 1-G(i1) complex*. Nature, 2019. **572**(7767): p. 80-85.
81. Qi, X., et al., *Cryo-EM structure of oxysterol-bound human Smoothed coupled to a heterotrimeric G(i)*. Nature, 2019. **571**(7764): p. 279-283.
82. Gao, Y., et al., *Structures of the Rhodopsin-Transducin Complex: Insights into G-Protein Activation*. Mol Cell, 2019. **75**(4): p. 781-790.e3.
83. Yin, W., et al., *A complex structure of arrestin-2 bound to a G protein-coupled receptor*. Cell Res, 2019. **29**(12): p. 971-983.
84. Tsai, C.J., et al., *Cryo-EM structure of the rhodopsin-Gai- $\beta\gamma$  complex reveals binding of the rhodopsin C-terminal tail to the  $g\beta$  subunit*. Elife, 2019. **8**.



**STable 1:** List of proteins included in the study. The table relates for each protein the Protein Data Bank (PDB) entry, the Electron Microscopy Database (EMD) entry, the release year, the symmetry employed, the overall resolution, the nature of the amphipathic compound used to solve the structure (final purification step), and the reference of the structure.

PROTEIN	PDB	EMD	YEAR	SYM.	RES. (Å)	Amphipathic compound	Reference
TRPV1	3J5P	5778	2013	C4	3.3	Amphipol	[19]
	3J5Q	5776	2013	C4	3.8	Amphipol	[20]
	3J5R	5777	2013	C4	4.2	Amphipol	[20]
	5IRX	8117	2016	C4	2.95	Nanodisc (MSP2N2)	[21]
	5IRZ	8118	2016	C4	3.28	Nanodisc (MSP2N2)	[21]
	5IS0	8119	2016	C4	3.4	Nanodisc (MSP2N2)	[21]
TRPV2	6U84	20677	2019	C4	3.7	Nanodisc (MSP2N2)	[22]
	5AN8	6455	2015	C4	3.8	Amphipol	[23]
	6O03	20143	2019	C4	2.9	Nanodisc (MSP2N2)	[24]
	6B04	7118	2018	C4	4.0	LMNG	[25]
	5HI9	6580	2016	C4	4.4	DMNG	[26]
TRPV3	6DVW	8919	2018	C4	4.3	Digitonin	[27]
	6DVY	8920	2018	C4	4.0	Digitonin	[27]
	6DVZ	8921	2018	C4	4.24	GDN	[27]
	6LGP	882	2019	C4	3.3	Nanodisc (MSP2N2)	[28]
	6MHO	9115	2018	C4	3.4	Poly (Maleic Anhydride-alt-1-Decene)/PMALC8	[29]
	6UW4	20917	2020	C4	3.1	Nanodisc (MSP2N2)	[30]
	6MHS	9117	2018	C4	3.2	Poly (Maleic Anhydride-alt-1-Decene)/PMALC8	[29]
	6UW6	20918	2020	C4	3.66	Nanodisc (MSP2N2)	[30]
	6UW9	20920	2020	C4	4.33	Nanodisc (MSP2N2)	[30]
	6UW8	20919	2020	C4	4.02	Nanodisc (MSP2N2)	[30]
	6PVL	20492	2019	C4	4.4	GDN	[31]
	6PVM	20493	2019	C4	4.5	GDN	[31]
	6PVO	20495	2019	C4	5.18	GDN	[31]
	6PVN	20494	2019	C4	4.07	GDN	[31]
	6PVP	20496	2019	C4	4.48	GDN	[31]
TRPV5	6B5V	7058	2017	C4	4.8	DMNG	[32]
	6O1N	593	2019	C4	2.9	Nanodisc (MSP2N2)	[33]
	6PBF	20292	2019	C4	4.2	Nanodisc (MSP2N2)	[32]
TRPV6	6D7T	7825	2018	C4	4.44	Amphipol	[34]
	6E2F	8961	2018	C1	3.9	Amphipol	[34]
	6E2G	8962	2018	C1	3.6	Amphipol	[34]
LRRC8A	5ZSU	6952	2018	C3	4.25	Digitonin	[35]
	6O00	564	2019	C6	4.18	Nanodisc (MSP1E3D1)	[36]
	6DJB	7935	2018	C3	4.4	Digitonin	[37]
TMEM16	6BGI	7095	2017	C2	3.8	Nanodisc (MSP2N2)	[38]
	6BGJ	7096	2017	C2	3.8	LMNG	[38]
V-ATPase	5TJ5	8409	2016	C1	3.9	Amphipol	[39]
	6C6L	7348	2018	C1	3.5	Nanodisc (MSP1E3D1)	[40]
	6O7T	644	2019	/	3.2	GDN	[41]
OTP3	6NF6	9361	2019	C2	3.3	Nanodisc (MSP2N2)	[42]
	6O84	650	2019	-	3.92	DDM CHS	[43]
OSCA	6MGV	9112	2018	C2	3.1	Nanodisc (MSP2N2)	[44]
	6OCE	20017	2019	C2	4.9	UDM-CHS	[45]
PKD TRP	5T4D	8354	2016	-	3.0	Nanodisc	[46]



	6A70	6991	2018	-	3.6	Digitonin	[47]
	5K47	8200	2016	-	4.2	UDM	[48]
	5MKF	3524	2017	-	4.2	Amphipol	[49]
	5MKE	3523	2017	-	4.3	Amphipol	[49]
MsbA	5TTP	8467	2017	C2	4.8	Nanodisc (MSP1D1)	[50]
	5TV4	8469	2017	C1	4.2	Nanodisc (MSP1D1)	[50]
Pgp	6QEE	4536	2019	C1	3.9	Nanodisc (MSP1D1)	[51]
	6C0V	7325	2018	C1	3.4	DDM-CHS	[52]
	6FN1	4281	2018	C1	3.58	Amphipol	[53]
	6FN4	4282	2018	C1	4.14	LMNG-CHS	[53]
	6QEX	4539	2019	-	3.6	Nanodisc (MSP1D1)	[51]
CFTR	6D3R	7793	2018	C2	4.30	Digitonin	[54]
	6MSM	9230	2018	-	3.20	Digitonin	[55]
	5UAK	8516	2017	-	3.87	Digitonin	[56]
	5UAR	8461	2016	-	3.73	-	[57]
	6O2P	0611	2019	-	3.3	-	[58]
	5W81	8782	2017	-	3.37	LMNG	[59]
MRP1	5UJ9	8559	2017	-	3.49	Digitonin	[60]
	5AUJ	8560	2017	-	3.34	Digitonin	[60]
	6BHU	7099	2017	-	3.14	Digitonin	[61]
TAP1/TAP2	5UJ9	8482	2017	-	3.97	C12E8	[62]
ABCG2	5NJG	3654	2017	-	3.78	Nanodisc (MSP1D1)	[63]
	6ETI	3953	2018	-	3.1	Nanodisc (MSP1D1)	[64]
	6FEQ	4246	2018	-	3.6	Nanodisc (MSP1D1)	[64]
	6FFC	4256	2018	C2	3.56	Nanodisc (MSP1D1)	[64]
	6HCO	0196	2018	C2	3.58	Nanodisc (MSP1D1)	[65]
	6HZM	0190	2018	C2	3.09	Nanodisc (MSP1D1)	[65]
ABCA1	5XJY	6724	2017	C1	4.10	Digitonin	[66]
LptB2FGC	6MI7	9125	2019	C1	4.2	Nanodisc (MSP1D1)	[67]
	6S8N	10125	2019	C1	3.10	LMNG	[68]
GPCR	5UZ7	8623	2017	C1	4.1	MNG/CHS	[69]
	6B3J	7039	2018	C1	3.3	MNG/CHS	[70]
	6CMO	7517	2018	C1	4.5	Digitonin	[71]
	6D9H	7835	2018	C1	3.6	LMNG/CHS	[72]
	6E3Y	8978	2018	C1	3.3	LMNG/CHS	[73]
	6G79	4358	2018	C1	3.78	DM	[74, 75]
	6N4B	0339	2019	C1	3	LMNG/GDN	[76]
	6NBF	0410	2019	C1	3	LMNG/GDN/CHS	[77]
	6NI3	9376	2019	C1	3,8	LMNG	[78]
	6OIJ	20078	2019	C1	3,3	LMNG/GDN	[79]
	6OIK	20079	2019	C1	3,6	LMNG/GDN	[79]
	6OS9	20180	2019	C1	3	LMNG/GDN	[80]
	6OT0	20190	2019	C1	3,84	MNG/GDN/ CHS/ Digitonin	[81]
	6OY9	20222	2019	C1	3,9	LMNG	[82]
	6PWC	20505	2019	C1	4,9	Digitonin	[83]
	6QNO	4598	2019	C1	4,38	/	[84]

**STable2:** Belt measurements for all entries listed in STable 1.

PROTEIN	PDB	EMD	Belt measurements (Å)					
TRPV1	3J5P	5778	22	20	16	15	14	14
	3J5Q	5776	25	24	23	22	21	20
	3J5R	5777	29	22	24	21	19	18
	5IRX	8117	33	29	28	16	15	15
	5IRZ	8118	36	32	32	17	17	14
	5IS0	8119	36	32	32	19	18	17
TRPV2	6U84	20677	40	41	36	20	23	22
	5AN8	6455	29	29	27	17	16	16
	6O03	20143	34	32	29	20	15	15
	6B04	7118	28	24	21	21	15	11
	5HI9	6580	24	25	22	15	15	14
TRPV3	6DVW	8919	28	23	22	21	19	17
	6DVY	8920	29	25	20	19	15	14
	6DVZ	8921	28	27	25	24	23	21
	6LGP	882	32	27	26	21	23	19
	6MHO	9115	35	32	25	23	21	17
	6UW4	20917	25	21	20	19	18	16
	6MHS	9117	24	20	19	18	17	15
	6UW6	20918	34	33	28	24	23	22
	6UW9	20920	28	24	21	20	19	18
	6UW8	20919	26	25	24	23	23	19
	6PVL	20492	25	23	23	22	21	16
	6PVM	20493	32	30	29	27	23	18
	6PVO	20495	29	23	22	21	20	19
	6PVN	20494	31	24	23	21	18	15
	6PVP	20496	35	31	29	22	21	19
TRPV5	6B5V	7058	25	21	20	18	16	15
	6O1N	593	35	34	27	17	15	14
	6PBF	20292	37	39	36	25	22	21
TRPV6	6D7T	7825	20	19	17	15	15	13
	6E2F	8961	41	31	25	24	22	20
	6E2G	8962	21	20	18	17	14	13
LRRC8A	5ZSU	6952	29	29	27	26	26	25
	6O00	564	37	34	35	32	32	30
	6DJB	7935	22	22	20	19	18	16
TMEM16	6BGI	7095	41	37	29	29	27	26
	6BGJ	7096	30	30	30	17	13	11
V-ATPase	5TJ5	8409	19	19	17	16	15	13
	6C6L	7348	20	18	18	16	15	12
	6O7T	644	24	24	20	19	19	18
OTP3	6NF6	9361	29	22	21	20	19	15
	6O84	650	30	30	27	27	27	26
OSCA	6MGV	9112	28	28	28	25	21	19
	6OCE	20017	36	34	33	31	30	30
PKD TRP	5T4D	8354	30	26	24	23	16	15
	6A70	6991	24	23	20	19	19	17
	5K47	8200	23	22	16	15	12	11
	5MKF	3524	17	15	14	13	13	10
	5MKE	3523	30	26	24	23	16	15
MsbA	5TTP	8467	28	24	22	20	20	16
	5TV4	8469	27	20	19	18	16	15
Pgp	6QEE	4536	44	42	38	37	36	32
	6C0V	7325	32	27	26	29	19	26
	6FN1	4281	40	35	35	35	35	31
	6FN4	4282	36	34	34	34	32	30

	6QEX	4539	32	30	30	29	28	24
BmrA	6R81	4749	20,9	19,8	14	13,7	13,1	13
CFTR	6D3R	7793	30	28	27	25	19	19
	6MSM	9230	35	31	30	29	29	24
	5UAK	8516	32	30	29	24	21	21
	5UAR	8461	43	41	33	29	28	25
	6O2P	0611	39	33	28	29	27	22
	5W81	8782	36	35	30	27	23	19
MRP1	5UJ9	8559	32	27	26	24	22	22
	5AUJ	8560	29	25	22	20	20	19
	6BHU	7099	27	26	24	21	21	14
TAP1/TAP2	5UJ9	8482	25	24	23	20	18	18
ABCG2	5NJG	3654	20	19	17	16	15	15
	6ETI	3953	19	19	17	16	14	14
	6FEQ	4246	31	31	27	25	22	22
	6FFC	4256	29	28	26	25	25	24
	6HCO	196	33	32	31	28	28	26
	6HZM	190	26	25	23	23	22	22
ABCA1	5XJY	6724	35	31	28	27	26	25
LptB2FGC	6MI7	9125	28	25	23	22	21	20
	6S8N	10125	22	19	18	18	16	14
GPCR	5UZ7	8623	36	30	28	27	22	21
	6B3J	7039	30	27	24	24	17	17
	6CMO	7517	35	32	32	30	30	28
	6D9H	7835	23	22	19	19	17	16
	6E3Y	8978	24	20	18	16	13	13
	6G79	4358	22	21	20	19	16	15
	6N4B	0339	29	27	26	26	25	24
	6NBF	0410	36	36	32	29	28	27
	6NI3	9376	21	19	19	18	17	16
	6OIJ	20078	26	26	23	20	20	19
	6OIK	20079	33	31	31	28	27	22
	6OS9	20180	25	25	24	23	20	18
	6OT0	20190	31	31	30	29	28	22
	6OY9	20222	24	24	24	21	20	16
	6PWC	20505	38	36	34	30	29	29
	6QNO	4598	21	17	16	15	15	13

**Title:** Nanodisc, amphipol or detergent belts in cryoEM reconstructions of membrane proteins are similar and correspond to a common ordered solvent layer

Veronica Zampieri<sup>1</sup>, Alexia Gobet<sup>1</sup>, Xavier Robert<sup>1</sup>, Pierre Falson<sup>1</sup>, Vincent Chaptal<sup>1\*</sup>

<sup>1</sup> Molecular Microbiology and Structural Biochemistry Laboratory (CNRS UMR 5086), University of Lyon, IBCP, 7, passage du Vercors, 69367 Lyon, France.

\* To whom correspondence should be addressed. [vincent.chaptal@ibcp.fr](mailto:vincent.chaptal@ibcp.fr)

## Supplementary Figures

